New Constraint on the ^{237}Np$(n,\gamma)^{238}$Np Integral Cross Section Using the Godiva-IV Critical Assembly

A. S. Tamashiro[1],* S. Burcher[1], J. T. Harke[1], B. Pierson[2], J. G. Duarte[1], Y. Mishnayot[1], S. W. Padgett[1], P. Zhao[1], N. Gharibyan[1], J. Goda[3], L. Greenwood[2], D. Hayes[3], J. Hutchinson[3], N. Harward[1], K. Roberts[1], G. Slavik[3], and J. Walker[3]

[1] *Lawrence Livermore National Laboratory, Livermore, CA 94550*

[2] *Pacific Northwest National Laboratory, Richland, WA 99354 and*

[3] *Los Alamos National Laboratory, Los Alamos, NM 87545*

(Dated: April 11, 2024)

Background: Accurate knowledge of the ^{237}Np$(n,\gamma)^{238}$Np cross section at fast neutron energies is important for applied nuclear science. The presently available experimental data has large disagreements in the fast neutron region.

Purpose: Perform a model-independent measurement of the ^{237}Np$(n,\gamma)^{238}$Np integral cross section using a well characterized fast neutron source and compare the result with previous measurements and current nuclear data evaluations. Provide an integral measurement that can be used as a benchmark for current evaluations.

Methods: Multiple samples of ^{237}Np were irradiated in the Godiva-IV critical assembly. Following the irradiation, the samples placed in a γ-ray counting setup and the γ-rays emitted from the decay of ^{238}Np were measured over a time period of approximately 7 days. Multiple γ-ray decay branches of ^{238}Np were observed.

Results: The observed activity of ^{238}Np was used to calculate the amount of ^{238}Np produced during the irradiation via the ^{237}Np$(n,\gamma)^{238}$Np reaction and an integral cross section of 342(11) *mb* was measured for the Godiva-IV neutron spectrum. The ^{238}Np half-life has been measured with a result of 50.31(5) hours.

Conclusion: The ^{237}Np$(n,\gamma)^{238}$Np integral cross section measured in this work is in agreement with overlapping 1σ error bands to ENDF/B-VIII.0. However, the measured value is 3σ away from the calculated integral cross section using JENDL-5. This measurement offers a reliable benchmark for future ^{237}Np$(n,\gamma)^{238}$Np cross section evaluations.

I. INTRODUCTION

Accurate neutron capture cross sections for major and minor actinides across a range of incident neutron energies are important for basic and applied nuclear science. With the ability to transmute actinides, neutron-capture reaction rates play an important role in understanding the population of different actinide species in high neutron flux environments, such as nuclear reactors. Full and accurate accounting of actinide species in simulations of nuclear reactors is crucial to the ability to make reliable design decisions based on the results of a simulation.

Integral measurements are often used as benchmarks for nuclear data, and therefore high-quality integral experiments with small and well understood uncertainties are of great value to the nuclear data community. However, the usefulness of integral measurements can be limited by large experimental uncertainties. In addition, integral measurements that are strongly reliant on modeling and therefore subject to the uncertainty of the model (neutron energy groups, geometry of setup, etc) are susceptible to the introduction of different systematic errors [1].

According to EXFOR, 16 entries used critical assemblies, 14 of which were integral cross section measurements using a metallic ^{235}U critical assembly [2]. The last integral cross section measurement was from 1986 for ^{243}Cm(n,f) [3]. This means the last critical assembly entry in EXFOR was almost four decades ago and none exist for ^{237}Np$(n,\gamma)^{238}$Np.

To date, there are two measurements for ^{237}Np$(n,\gamma)^{238}$Np integral cross section in the fast or fission regime. The first measurement was conducted in 1983 by Cricchio et. al. at the Rapsodie Fortissima reactor resulting in 640(70) mb [4]. The experiment irradiated solution samples to then be chemically separated and measured using mass spectrometry. Rapsodie Fortissima reactor was a sodium-cooled fast reactor, which would have some moderation from neutrons scattering off of the sodium coolant. The second measurement was conducted in 1991 by Zvonarev et. al. at the BR-1, as known as Brystry Reactor-1, fast reactor resulting in a ratio of $(^{237}\mathrm{Np}(n,\gamma))/(^{235}\mathrm{U}(n,f))$ = 0.240(12) [5]. BR-1 was a fast nuclear reactor fueled by metallic plutonium fuel rods, which would provide fission spectrum neutrons. The samples were irradiated and γ-ray spectroscopy was performed using Ge(Li) detectors.

The application of integral measurements is to model the experiment into a benchmark for nuclear data validation. The BR-1 experiment was simulated by D. Heinrichs [6] using COG [7], a Monte Carlo radiation transport code developed at Lawrence Livermore Na-

* Corresponding author: tamashiro1@llnl.gov

tional Laboratory. The calculations were performed using ENDF/B-VIII.0 (ENDF) library [8] (same as JEFF-3.3 [9]). The ratio of calculated to experimental results for $(^{237}\mathrm{Np}(n,\gamma))/(^{235}\mathrm{U}(n,f))$ was 1.228 ± 0.064, which indicated that the ENDF library is biased high for the $^{237}\mathrm{Np}(n,\gamma)$ cross section.

Figure 1 shows a compilation of experimental results for ^{237}Np(n,γ) cross sections found in EXFOR (Experimental Nuclear Reaction Data) [2] overlayed on evaluated data from ENDF and JENDL-5 (JENDL) [10]. ENDF and JENDL agree with each other until around the highest neutron energy measured at 2.73 MeV. Both database diverge in higher neutron energies, which can be explained by different evaluation styles and how nuclear cross sections are calculated with the absence of measured results.

Within the Device Assembly Facility (DAF) at the Nevada National Security Site (NNSS), this work utilized the Godiva-IV critical assembly operated by Los Alamos National Laboratory (LANL) as part of the National Criticality Experiments Research Center (NCERC). Godiva IV is comprised of metallic uranium fuel with 1.5% Mo to provide fission spectrum neutrons [24]. Samples of ^{237}Np were irradiated and γ counted within one hour after irradiation. The presence of ^{238}Np γ-rays allowed for the analysis of ^{238}Np half-life and unprecedented $^{237}\mathrm{Np}(n,\gamma)$ integral cross section measurement using Godiva IV. Results were compared to calculated ENDF and JENDL integral cross sections.

II. EXPERIMENT

A. ^{237}Np Sample Preparation

A total of four ^{237}Np-nitrate samples were prepared at Lawrence Livermore National Laboratory (LLNL). The four samples contain masses of ^{237}Np ranging from 6.0(1) to 44.5(4) mg. The mass of ^{237}Np in the samples was determined by the activity prior to irradiation, as measured via γ-ray spectroscopy. Due to the low energy of the emitted γ-rays, to accurately determine the activity, a correction for the self-attenuation was performed and it is described in Section II C.

To prepare the samples, neptunium oxide (NpO_2) powder was dissolved in nitric acid (HNO_3) and the solution was diluted with isopropyl alcohol. The solution was then micropipetted into single ended quartz tubes. The tubes were placed on a hot plate located inside a fume hood and baked. During the baking, the alcohol evaporated away leaving behind Neptunium nitrate ($NpO_2(NO_3)$). More solution was added to the tubes in repetition until the approximate desired mass was achieved. The quartz tubes containing the samples were then flame-sealed to prevent the escape of gaseous fission products. The quartz tubes had a wall thickness of 0.5 mm.

B. Irradiation with Godiva-IV

The Neptunium samples and a witness foil pack were irradiated in the Godiva-IV critical assembly on January 22, 2020. Godiva IV is an unreflected highly-enriched uranium (HEU) cylindrical critical assembly with an internal cavity 0.55 inches in diameter used to expose experimental samples to a high neutron flux. Samples are loaded into a thin aluminum tube that is inserted into the center cavity. The Godiva-IV neutron spectrum is not the pure ^{235}U fission spectrum but a slightly degraded spectrum due to neutron down-scatter. For this experiment Godiva-IV was operated in burst mode, and the super-prompt neutron irradiation lasted approximately 54 μsec FWHM inside the central cavity. The short duration of the irradiation time when compared to the half-life of the activation product of interest, ^{238}Np, allows for the irradiation to be treated as instantaneous.

The dynamic behavior of the super-prompt critical transient was monitored by measuring optical photon fluorescence induced by radiation emitted from the critical assembly by two optical monitors: a photo-multiplier tube (PMT) and a photo-diode (PD). The PMT provided much higher signal gain than the PD and was used for higher temporal fidelity of the initial reactivity transient before the onset of heating and thermo-mechanical expansion. The PD operated with much lower signal gain and was used to follow the entire transient from beginning to end. The time difference between the leading edge half-max to max was used as a measure of the transient length. Figure 2 is a plot of the PMT and newer PD signal as measured during the burst. The signal rise from 1 to 5 volts in the PMT is fit using Equation 1 to estimate the transient reactivity period from α, a fit parameter [25]. In an applied sense, this period represents the growth rate of the neutron population, $n(t)$, at the start of the transient. The time-dependence of the growth rate of the radiation field around the critical assembly measured before these physical effects perturb the neutron population provide an initial estimate of the core reactivity before the excursion. However, this over-simplified model does not account for the effects of thermo-mechanical shock or the sudden drop in reactivity produced by the safety block dropping out of the core on the neutron population. Hence the use of only the PMT data to make this initial estimate.

$$n(t) = n_o \cdot e^{\alpha t} \tag{1}$$

The initial reactivity period was measured to be 14.70±0.06 μsec with a residual-χ^2 of 0.461 using the precision of the measured voltage, ±0.2 volt, as the uncertainty for each measured voltage data point. This uncertainty is likely over-estimated as voltage measurements were taken every 20 nsec such that multiple voltage measurements between each 0.2 volt step were recorded, representing an average estimate with higher precision than 0.2 volts. Reducing the uncertainty from 0.2 to 0.14

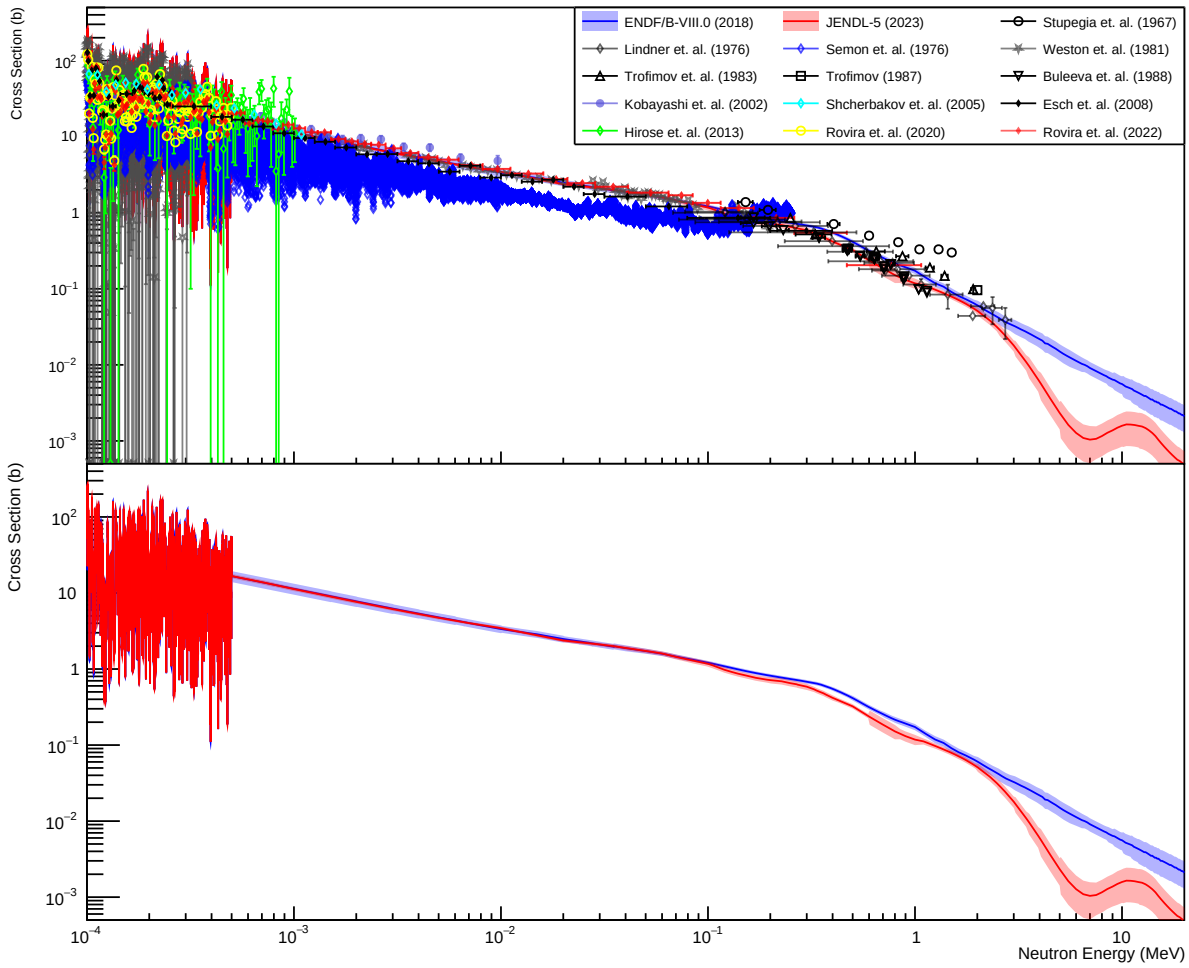

FIG. 1: Shown are the evaluated ^{237}Np(n,γ) cross section from ENDF and JENDL. Overlayed are experimental values from Stupegia et. al. [11], Lindner et. al. [12], Semon et. al. [13], Weston et. al. [14], Trofimov et. al. [15], Trofimov [16], Buleeva et. al. [17], Kobayashi et. al. [18], Shcherbakov et. al. [19], Esch et. al. [20], Hirose et. al. [21], Rovira et. al. [22], and Rovira et. al. [23].

increases the residual-χ^2 to 1 and reduces the uncertainty in the measured period to 0.04 μsec. The correlation between number of fissions in the assembly core and the initial reactor period developed by Wimmet, et al. [26] indicates nearly 3×10^{16} total fissions occurred during the burst. The temperature is also tracked as a function of time during the transient to estimate the maximum temperature observed at the center of the core. This metric is also used to estimate the magnitude of the burst. A peak temperature of 151.1 °C was measured following the burst.

C. γ-ray Counting

The γ-ray counting setup consists of two Broad-Energy Germanium (BEGe) detectors (Canberra, model BE6530) mounted on large liquid nitrogen dewars. The two detectors are oriented such that they are 18 cm apart facing each other. The active volume of the two detectors is surrounded by box-like construction of lead bricks with a 1 cm layer of copper lining the internal walls. A photograph of the setup is shown in Figure 3. A fixed sample holder is located inbetween the two detectors to allow for reproducible placement of samples and calibration sources. The face of each detector is covered with 0.159 cm thick stainless-steel and 1.5 cm Teflon disks to reduce background due to X-rays and β-particles.

The data acquisition system (DAQ) consisted of two Canberra Lynx modules, one for each detector, connected to a computer. The pulse height of events measured in the detectors were written to two separate files in list mode with a time stamp from the computer. The live time of the data acquisition system ranged from approximately 77% at the beginning of counting to 82.5% over the week of counting as the activity due to fission prod-

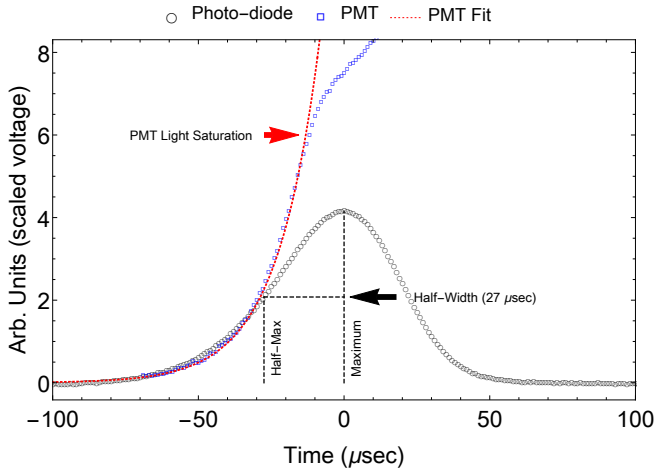

FIG. 2: Reactivity transient time-dependence as measured from radiation induced fluorescence around the Godiva-IV critical assembly using a PMT and PD.

FIG. 3: Detector setup in LLNL building near the Godiva-IV building. This photo was taken during the July 2015 campaign.

ucts created by neutron induced fission of ^{237}Np had decayed away.

The γ-ray detection efficiency and energy calibration of the two BEGe detectors was characterized using standard γ-ray check sources with known activity. The sources used for the efficiency measurement were ^{60}Co, ^{137}Cs, ^{22}Na, ^{133}Ba, and ^{152}Eu. The reference activity for the sources was provided by the manufacturer, Eckert & Ziegler, and was reported to have a 3% relative uncertainty for all of the sources. Each source was measured individually for a time ranging from 5 to 10 minutes. The sources were secured inside the sample holder and aligned such that they were at the same position with respect to the two detectors as the ^{237}Np sample was during data collection. The results of the efficiency characterization for each detector individually is shown in the upper panel of Figure 4. The data in Figure 4 has been

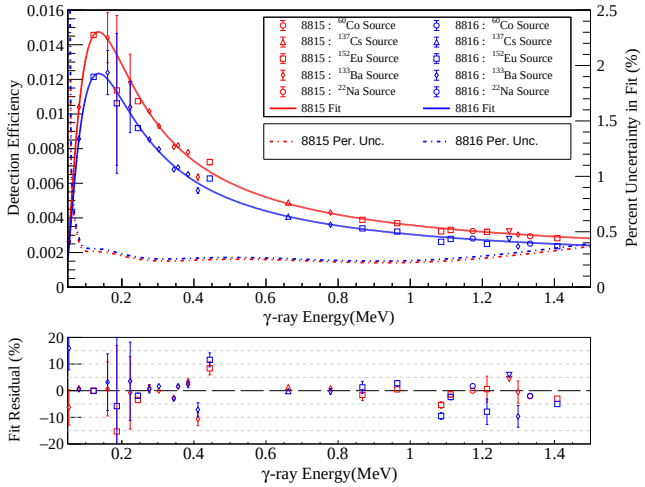

FIG. 4: The measured efficiency versus γ-ray energy. The red points are for detector 8815 (upper) and the blue points are for detector 8816 (lower). The different shape points correspond to the different sources used for the measurements. Equation 2 is used for the detector efficiency fit, resulting in the curves in the upper panel. The shaded bands represent the uncertainty in the fit function. The lower panel shows the residuals to the fits.

fit using Equation 2, where P_i are free parameters and E_γ is γ-ray energy in MeV. The residuals for the fit are shown in the lower panel.

$$\varepsilon(E_\gamma) = P_0 E_\gamma^{-P_1} + P_2 - P_3 e^{-P_4 E_\gamma} \quad (2)$$

The parameters 0–4 were extracted from the efficiency fit (see Table I). The uncertainty was calculated using the following ROOT [27] generated covariance matrices:

	P_0	P_1	P_2	P_3	P_4
P_0	1.4E-9	-3.8E-7	-1.4E-9	-1.3E-7	-1.6E-6
P_1	-3.8E-7	1.1E-4	3.6E-7	3.6E-5	3.5E-4
P_2	-1.4E-9	3.6E-7	1.4E-9	1.2E-7	1.6E-6
P_3	-1.3E-7	3.6E-5	1.2E-7	1.3E-5	1.3E-4
P_4	-1.6E-6	3.5E-4	1.6E-6	1.3E-4	5.6E-3

	P_0	P_1	P_2	P_3	P_4
P_0	1.0E-9	-3.3E-7	-1.0E-9	-9.5E-8	-1.7E-6
P_1	-3.3E-7	1.1E-4	3.1E-7	3.3E-5	4.5E-4
P_2	-1.0E-9	3.1E-7	1.0E-9	8.9E-8	1.6E-6
P_3	-9.5E-8	3.3E-5	8.9E-8	1.0E-5	1.4E-4
P_4	-1.7E-6	4.5E-4	1.6E-6	1.4E-4	6.6E-3

for detectors 8815 and 8816 respectively. The error analysis of detector efficiency is discussed in Appendix A.

III. ANALYSIS

The ^{237}Np$(n,\gamma)^{238}$Np cross section is given by Equation 3. In this work, the total neutron fluence (Φ_n), the

TABLE I: Efficiency curve parameters.

P_i	Detector 8815	Detector 8816
[0]	$2.18 \times 10^{-3} \pm 4 \times 10^{-5}$	$1.80 \times 10^{-3} \pm 3 \times 10^{-5}$
[1]	1.08 ± 0.01	1.09 ± 0.01
[2]	$1.41 \times 10^{-3} \pm 4 \times 10^{-5}$	$1.23 \times 10^{-3} \pm 3 \times 10^{-5}$
[3]	0.210 ± 0.004	0.178 ± 0.003
[4]	26.63 ± 0.07	26.44 ± 0.08

number of ^{237}Np atoms in the sample ($N_{^{237}\mathrm{Np}}$), and the number of ^{238}Np atoms in the sample following the irradiation ($N_{^{238}\mathrm{Np}}$), are all determined experimentally. Section III A, Section III B, and Section III C describe the procedures for measuring the total neutron fluence during the irradiation, the amount of ^{237}Np in the samples prior to irradiation, and the amount of ^{238}Np produced during the irradiation, respectively.

$$\sigma_{(n,\gamma)} = \frac{N(^{238}\mathrm{Np})}{\Phi_n \; N(^{237}\mathrm{Np})} \tag{3}$$

A. Witness Foil Analysis

The fluence-energy profile of the irradiation was evaluated using simulation code MCNP 6.2 [28], measured activation products in the high-purity fluence monitor materials, and neutron spectral adjustment code STAYSL_PNNL [29]. A high-fidelity core model similar to the International Critical Experiments Benchmark Evaluation Program HEU-MET-086 evaluation [30] was used to model the neutron fluence energy profile inside the experimental cavity with a 100-group energy bin structure spanning from 10^{-10} MeV to 20 MeV in neutron energy. The activated fluence monitors were measured using calibrated gamma spectroscopy to measure the specific-activity of activation products within the high-purity materials. The measured specific-activity was then used to estimate the sum-product of the unknown fluence-energy neutron spectrum and known activation cross-section taken from the International Reactor Dosimetry Fission Fusion (IRDFF) cross-section library version 1.02 [31]. Table II presents the materials, masses, and measured reaction-rates per atom for reference. The associated gamma-lines, branching ratios, half-lives and corresponding uncertainties are given in Table III.

These measured specific-activation rates are provided as input to STAYSL_PNNL [29] along with the IRDFF [32] evaluated cross sections and simulated neutron fluence-energy profile from MCNP 6.2 [28] to perform a linear least-squares regression on the difference between the measured and predicted specific activation rates. Adjustments are made to the input neutron spectrum and estimated fluence covariance matrix to minimize the difference between the measured and model predicted neutron spectrum. Figure 5 is a plot of the neutron

TABLE II: Fluence monitor materials, masses, measured reaction rates and uncertainties. The reaction rate $< \sigma\phi >$ is listed in units of atoms of reactant produced per atom of target per second.

Material	Mass (mg)	Reaction	$< \sigma\phi >$	±%
Au	106.210	^{197}Au(n,γ)^{198}Au	3.559×10^{-11}	2
		^{197}Au(n,2n)^{196}Au	5.649×10^{-13}	2
Ti	81.958	^{46}Ti(n,p)^{46}Sc	1.753×10^{-12}	2
		^{47}Ti(n,p)^{47}Sc	2.978×10^{-12}	2
		^{48}Ti(n,p)^{48}Sc	4.930×10^{-14}	2
Fe	108.108	^{54}Fe(n,p)^{54}Mn	1.239×10^{-11}	2
		^{54}Fe(n,α)^{51}Cr	1.187×10^{-13}	8
		^{56}Fe(n,p)^{56}Mn	1.695×10^{-13}	2
		^{58}Fe(n,γ)^{59}Fe	7.260×10^{-13}	5
Co	28.635	^{59}Co(n,γ)^{60}Co	2.103×10^{-12}	2
Cu	100.225	^{63}Cu(n,γ)^{64}Cu	3.608×10^{-12}	3
		^{63}Cu(n,α)^{60}Co	8.363×10^{-14}	3
Ni	31.678	^{58}Ni(n,p)^{58}Co	1.576×10^{-11}	2
		^{60}Ni(n,p)^{60}Co	9.946×10^{-14}	13
Al	33.368	^{27}Al(n,α)^{24}Na	3.361×10^{-13}	2

TABLE III: Activation reaction nuclear data and uncertainties.

Reaction	E_γ (keV)	I_γ (%)	$t_{1/2}$
^{197}Au(n,γ)^{198}Au	411.80	95.62(6)	2.6941(2) d
^{197}Au(n,2n)^{196}Au	355.73	87.0(8)	6.167(1) d
^{46}Ti(n,p)^{46}Sc	889.27	99.984(1)	83.79(4) d
^{47}Ti(n,p)^{47}Sc	159.35	68.3(4)	3.3492(6) d
^{48}Ti(n,p)^{48}Sc	983.52	100.0(6)	43.67(9) h
^{54}Fe(n,p)^{54}Mn	834.84	99.976(1)	312.05(4) d
^{54}Fe(n,α)^{51}Cr	320.08	9.91(5)	27.704(3) d
^{56}Fe(n,p)^{56}Mn	846.76	98.85(10)	2.5789(1) h
^{58}Fe(n,γ)^{59}Fe	1099.24	56.5(18)	44.495(9) d
^{59}Co(n,γ)^{60}Co	1173.22	99.850(7)	1925.28(14) d
^{63}Cu(n,γ)^{64}Cu	1345.77	0.475(11)	12.701(2) h
^{63}Cu(n,α)^{60}Co	1173.22	99.850(7)	1925.28(14) d
^{58}Ni(n,p)^{58}Co	810.75	99.450(4)	70.86(6) d
^{60}Ni(n,p)^{60}Co	1173.22	99.850(7)	1925.28(14) d
^{27}Al(n,α)^{24}Na	1368.62	99.9936(15)	14.9970(12) h

spectrum as modeled and adjusted based on witness foil activities. The two are in excellent agreement with the adjustment deviations not exceeding 15% across the entire energy range. The spectrum observed by the samples is slightly softer than the model predicted spectrum during this experiment. The STAYSL_PNNL [29] evaluation improves the precision of the neutron spectrum by incorporating experimental conditions not always captured in the model.

The total neutron fluence to the samples during the burst was determined to be $\Phi_n = 2.86(7) \times 10^{14}$

neutrons/cm^2 using STAYSL. The flux-weighted mean neutron energy observed by the target was 1.34 MeV.

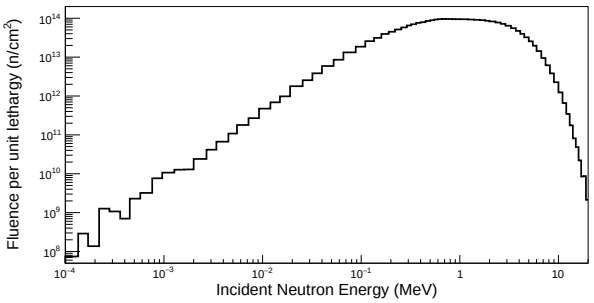

FIG. 5: A plot of the neutron fluence per unit lethargy as modeled and corrected using known activation reaction cross-sections. Lethargy is defined as $u = \ln(E_{n+1}/E_n)$ and is only intended for visual representation. The analysis used the neutron fluence, not the neutron fluence per unit lethargy.

B. ^{237}Np Activity Analysis

The isotope ^{237}Np is a long-lived isotope that emits different γ-rays. Therefore, each sample has an initial activity that can be measured via γ-ray spectroscopy utilizing the experimental setup described in Section II C. A representative γ-ray spectrum from the irradiated ^{237}Np samples is shown in Figure 6. The γ-rays emitted from ^{237}Np are labeled with red triangles. The γ-rays emitted in the decay of ^{237}Np used in this analysis are listed in Table IV along with the associated decay intensities and uncertainties. Other γ-rays from the decay of ^{237}Np were observed in this measurement. However, due to a combination of multiple unresolved interfering γ-rays and small branching ratios, fits of these peaks in the γ-ray spectrum were unreliable and therefore these γ-rays were excluded from this analysis.

Peaks in the γ-ray spectrum shown in Figure 6 were fit using a Gaussian with a linear background. The observed activity from a γ-ray peak was calculated using Equation 4, where C is the area of the Gaussian component of the peak, ε_γ is the γ-ray detection efficiency, R_γ is the decay branching ratio, and t_{live} is the live time of the data acquisition system during the count.

$$A_{obs} = \frac{C}{\varepsilon_\gamma \; R_\gamma \; t_{live}} \tag{4}$$

The observed activity from each γ-ray requires an energy-dependent correction for the attenuation of intensity due to shielding from the sample itself, referred to as self-attenuation. The observed intensity as a function of the γ-ray energy is described by Equation 5, where I_0 is the un-attenuated intensity and x is the average areal density of the material a photon traverses on its way out of the sample. The term $\mu(E_\gamma)$ is the energy dependent mass attenuation coefficient for the material. For this analysis we used the mass attenuation coefficients provided in the NIST XCOM database [33].

$$I(E_\gamma) = I_0 e^{-\mu(E_\gamma)x} \tag{5}$$

To determine the true activity of the ^{237}Np samples, the observed activity from γ-rays emitted in the decay of ^{237}Np are plotted as a function of γ-ray energy. These plots are shown in Figure 7 (a) and 7 (c) for Detectors 8815 and 8816 respectively. The observed activity versus γ-ray energy is then fit using Equation 5, with x and I_0 left as free parameters. The value of I_0 returned from the fit is the unattenuated activity of the sample, and the observed activities can be corrected using Equation 6, where F_{sa} is given by $F_{sa} = I(E_\gamma)/I_0$. Figure 7 (b) and 7 (d) show the results of applying Equation 6 to the observed activity. The dotted lines in these figures represent the value of I_0 returned from the fit.

$$A_{corr} = \frac{A_{obs}}{F_{sa}} \tag{6}$$

TABLE IV: The observed γ-rays from the ^{237}Np samples that were used for the self-attenuation correction and activity measurement. The decay intensity I_γ and associated uncertainty used for this analysis are listed. Other γ-rays were observed but due to multiple γ-rays interfering and/or small branching ratios they were excluded from this analysis.

Parent Isotope	E_γ (keV)	R_γ (%)
^{237}Np	134.3	0.072(3)
^{237}Np	151.4	0.244(3)
^{237}Np	194.7	0.182(5)
^{237}Np	212.3	0.152(3)
^{237}Np	214.0	0.0357(3)

The inclusion of many γ-rays with different energies in the analysis allowed for a more robust determination activity of the samples. The activities measured from detector 8815 and 8816 were found to be 672(18) kBq and 682(19) kBq, respectively, corresponding to masses of 25.8(7) mg and 26.2(7) mg of ^{237}Np.

C. ^{238}Np Decay Analysis

The entire summed γ-ray spectrum from the approximately 7 days of counting is shown in Figure 8. The γ-ray data was recorded in list mode and then binned into one hour time bins. The upper panel of Figure 9 shows the time binned data with counting time on the vertical

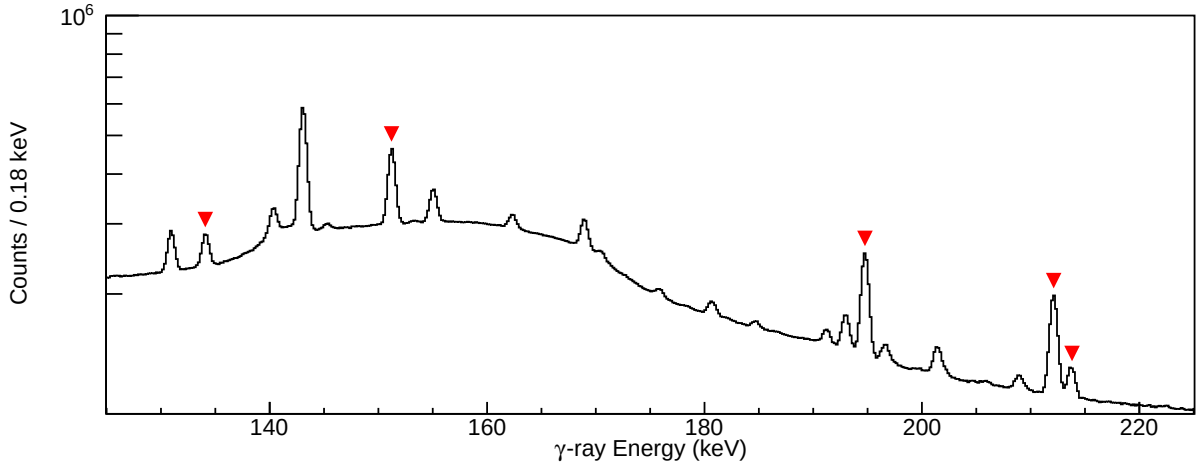

FIG. 6: The observed γ-ray spectrum from the ^{237}Np samples. The γ-rays used in this analysis from ^{237}Np are identified with red triangles. This data is the last ten hours of measurement of a seven day measurement after irradiation.

axis and γ-ray energy on the horizontal axis. The lower panel of Figure 9 shows a time-ordered series of projections of individual time bins on to the γ-ray energy axis. Viewing the data in this way highlights the time dependence of interfering γ-rays, that is not apparent in the summed spectrum shown in Figure 8. A total of 8 γ-rays emitted in the decay of ^{238}Np were used in this analysis. These γ-ray peaks are labeled with the numbered black arrows in Figure 8 and Figure 9 also listed in Table V. The use of a large set of γ-rays in this type of analysis reduces the sensitivity to a single imprecise decay branching ratio or unidentified interfering γ-ray and therefore provides a more robust measurement of the activity than measurements based on single γ-rays.

The amount of ^{238}Np produced via the ^{237}Np$(n,\gamma)^{238}$Np reaction during the irradiation in Godiva is determined by observing the activity of ^{238}Np over the post-irradiation counting time, fitting the activity as a function of time, and extrapolating back to the time of irradiation. In the γ-ray spectra from each one hour time bin, the γ-ray peaks of interest are fit with a Gaussian on a linear background. In the cases where interfering γ-ray peaks are present and the separation between the peaks is bigger than the energy resolution of the detector, more Gaussians are added to the fitting function as needed. The red arrows in Figure 8 and Figure 9 indicate the interfering γ-ray peaks that were included in the fits of the peaks of interest in order to produce reliable results.

The resolution of the γ-ray detectors as a function of energy was characterized to constrain fits of multiple unresolved peaks. The relation between the Gaussian width σ and the γ-ray energy E_γ was found to be well represented by Equation 7. A large sample of cleanly separated peaks in the post-irradiation γ-ray spectrum spanning a wide range of γ-ray energy were identified. The width of these peaks versus γ-ray energy was fit using Equation 7, with the parameters s_0 and s_1 as free parameters. The width of all γ-ray peaks fit in this analysis was then required to obey Equation 7 within 10 % of the resulting curve. In addition, the centroid of the peaks were confined to ± 0.1 keV of the peak energy in the final analysis. Peak energies were determined through an iterative process in which the allowed energy window was narrowed and the expected centroid value was refined repeatedly until the chi-square of the fits was found to be at a minimum and the resulting intensity versus time plot exhibited the exponential decay behavior expected from a radioactive source. Including these width and energy requirements in multi-peak fits was found to greatly improve the quality of the results.

$$W(E_\gamma) = s_0 + s_1 \sqrt{E_\gamma} \tag{7}$$

The area of a peak of interest is corrected for the live time of the DAQ in that time bin and plotted as function of time, with zero time set as the time of the irradiation. The intensity of the peaks of interest for this measurement versus time are shown in Figure 10. If the reduced chi-square of the peak fit exceeded a predetermined limit or if the peak area was less than 100 counts, the resulting intensity from the fits of individual spectra was considered poor and excluded from the intensity versus time fit.

The intensity of each peak of interest as a function of time is fit using Equation 9. Where Equation 9 is the result of the integration of the standard radioactive decay equation, $A(t) = A_0^{meas} e^{-\lambda t}$, over a time window $\Delta t = t_2 - t_1$, as shown in Equation 8. Due to the extremely short duration of the irradiation (54 μsec) compared to the half-life of ^{238}Np ($t_{1/2}$ = 2.099(2) d) and the size of the counting time bins (1 h), the irradiation can be

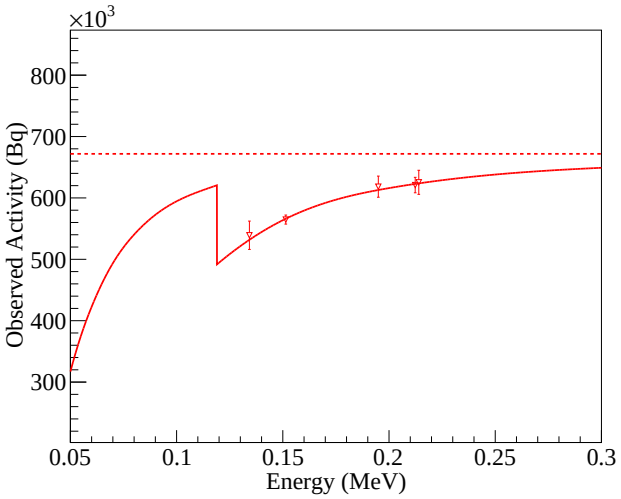

(a) Detector 8815 observed activity for each γ-ray listed in Table IV.

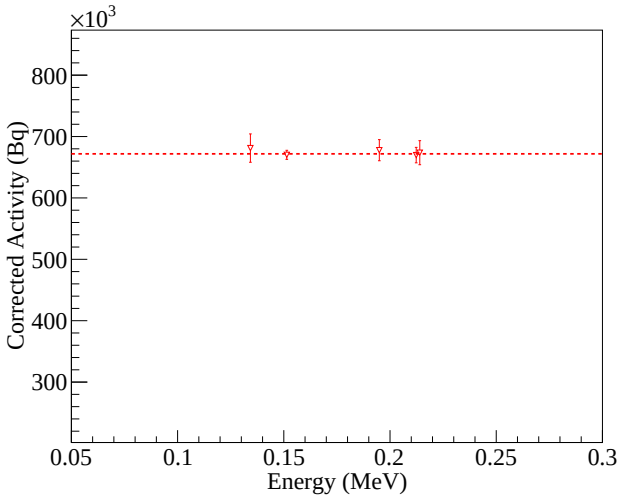

(b) Detector 8815 corrected activity for each γ-ray listed in Table IV.

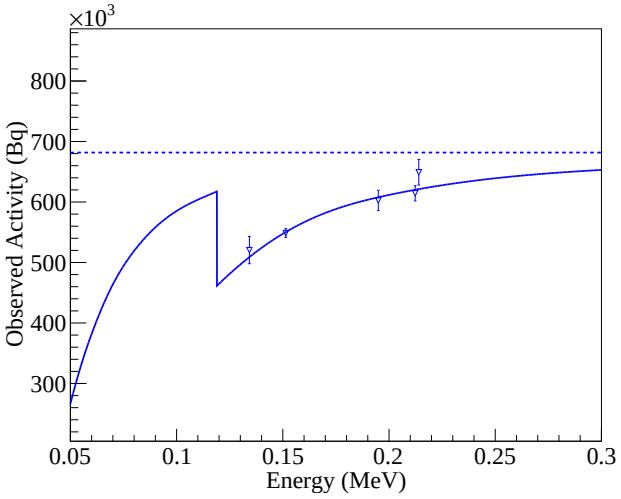

(c) Detector 8816 observed activity for each γ-ray listed in Table IV.

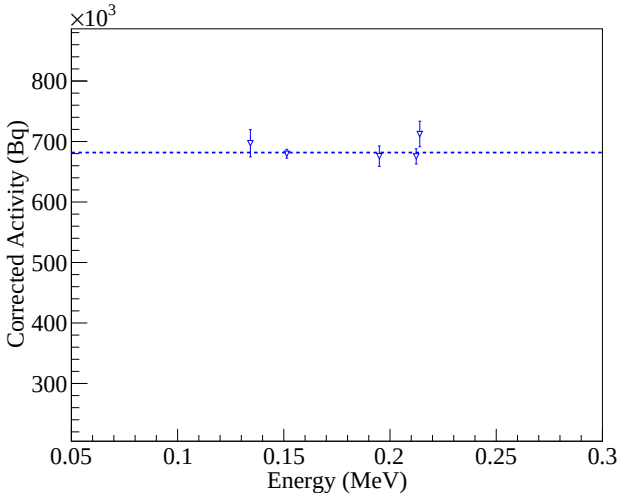

(d) Detector 8816 corrected activity for each γ-ray listed in Table IV.

FIG. 7: The observed and corrected activities for Detectors 8815 and 8816. In Panels (a) and (c) the observed activity for each γ-ray used in the analysis is plotted as a function of γ-ray energy. In Panels (b) and (d) the activity for each γ-ray is shown after being corrected for the attenuation of the sample. The solid-line curves in Panels (a) and (c) represent a fit to the data using Equation 5 with x and I_0 left as free parameters, as described in Section II C. The dotted lines in all panels are drawn at the value of I_0 extracted from the fits and represent the true activity of sample.

treated as approximately instantaneous and therefore no source is included in the radioactive decay equation $A(t)$.

$$C(t_1, t_2) = \int_{t_1}^{t_2} A(t)dt = \int_{t_1}^{t_2} A_0^{meas} e^{-\lambda t} dt \qquad (8)$$

$$C(t_1, t_2) = \frac{A_0^{meas}}{\lambda} e^{-\lambda t_2} \left(e^{\lambda \Delta t} - 1 \right) \qquad (9)$$

For this analysis both the initial activity A_0^{meas} and the decay constant λ were left as free parameters in the fit of the decay curves. The decay curves and corresponding fit results for the 8 γ-rays used in this analysis are shown in Figure 10. The normalized residuals for each decay curve fit are plotted in Figure 11. In the fit of the decay curves, certain time regions were excluded to large deviations from the expected exponential decay curve. These deviations were identified using the normalized residual

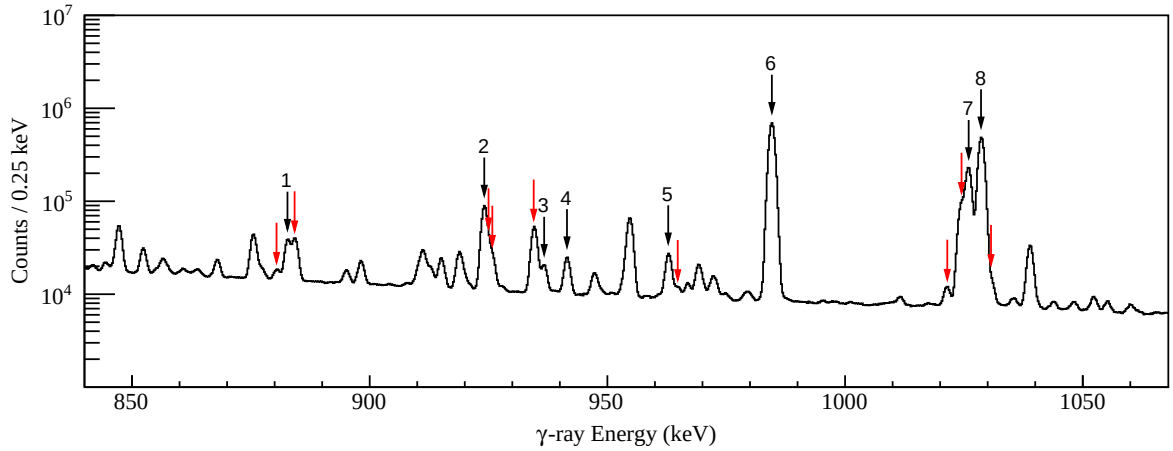

FIG. 8: Total γ-ray spectrum from the approximately 7 days of counting. The black arrows indicate the peaks from the decay of ^{238}Np and the red arrows indicate interfering γ-rays which were included in the multi-Gaussian fits. The numbered labels on the black arrows correspond to the peak number in Table V.

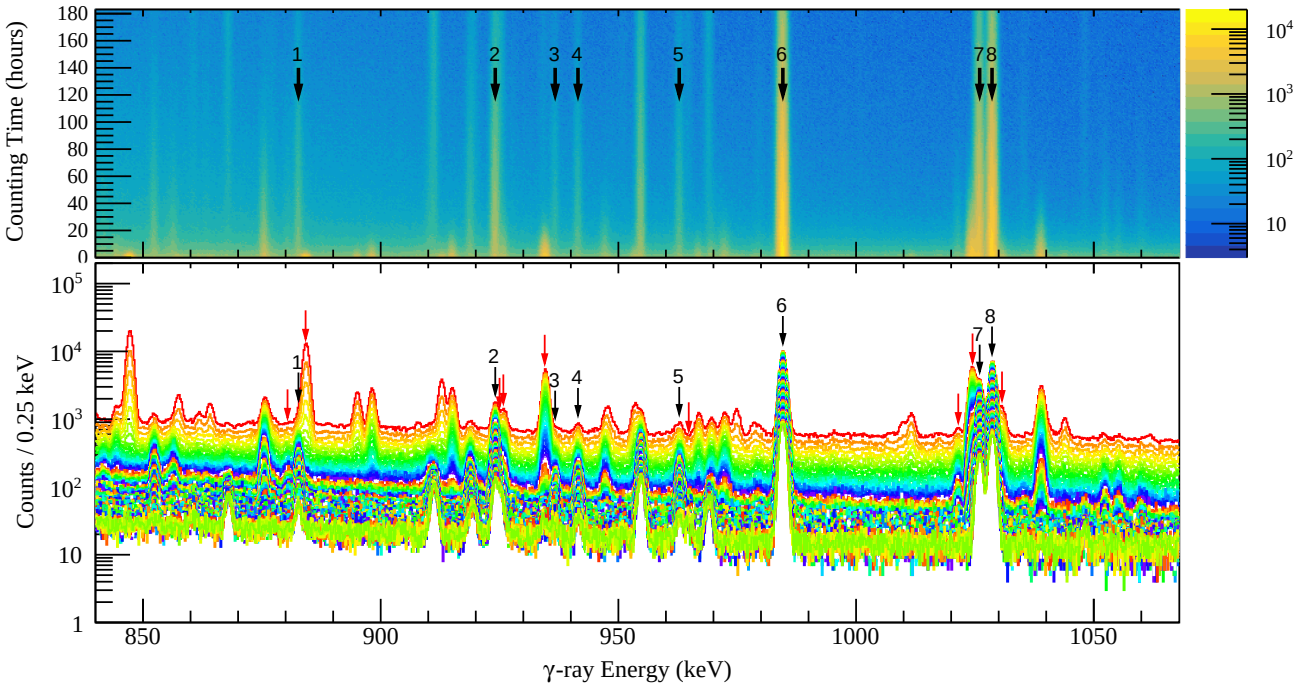

FIG. 9: The upper panel shows the region of the γ-ray energy versus counting time, the γ-rays from the decay of ^{238}Np used in this analysis are indicated with black arrows. The lower panel shows the projection of individual time bins on to the γ-ray energy axis. Viewing the data in this way allows for the identification of interfering γ-rays and provides a qualitative view of their time dependence. The red arrows in the lower panel indicate interfering γ-rays that could not be fully resolved from the peaks of interest and therefore were included in multi-Gaussian fits of the spectra in each time bin.

plots shown in Figure 11, and the excluded time bins are shown in red points. The source of the deviations is likely unresolved interfering γ-rays that could not be accounted for in the fits. The initial activity of ^{238}Np, A_0^{meas}, is extracted from the fit and then corrected for the γ-ray detection efficiency (ε_γ), the specific decay branching ratio (R_γ), and self-attenuation (F_{sa}) using Equation 10. A_0 is the resulting activity immediately following the irradiation moment at t=0

$$A_0 = \frac{A_0^{meas}}{\varepsilon_\gamma \; R_\gamma \; F_{sa}} \tag{10}$$

IV. RESULTS & DISCUSSION

For the calculation of the ^{237}Np$(n,\gamma)^{238}$Np integral cross section, the activity of ^{237}Np, the activity of ^{238}Np, the half-life of ^{238}Np, and total neutron fluence were all measured in this experiment. The half-life of ^{237}Np was not measured in this work, and therefore the ENSDF value of $2.14(7) \times 10^6$ years was used. The total neutron fluence during the burst was determined to be $\Phi_n = 2.86(7) \times 10^{14}$ neutrons/cm^2 using STAYSL. The integral cross section was calculated using Equation 11 individually for each of the 8 γ-rays included in this analysis. The measured half-life and integral cross section values for each γ-ray are shown in Figure 12 and listed in Table V.

$$\sigma_{(n,\gamma)} = \frac{A(^{238}\text{Np}) \; t_{1/2}(^{238}\text{Np})}{\Phi_n \; A(^{237}\text{Np}) \; t_{1/2}(^{237}\text{Np})} \tag{11}$$

For the weighted means, the parameters were ordered by γ-ray energy index i and detector index j. The uncertainty ($\Delta\sigma_{ij}$) for the measured integral cross sections (σ_{ij}) were calculated using error propagation. These values were listed under columns σ_{8815} and σ_{8816} of Table V. The weighted-mean under column σ_{mean} was calculated by the following:

$$\bar{\sigma} = \sum_i \sum_j W_{ij}\sigma_{ij}, \tag{12}$$

where $W_{ij} = \omega_{ij} / \sum_i \sum_j \omega_{ij}$ and $\omega_{ij} = 1/\Delta\sigma_{ij}^2$. However, for each γ-ray row, there was only one γ-ray to analyze. Equation 12 was expanded to be:

$$\bar{\sigma} = \sum_i \sum_j \frac{W_{ij} A_{ij}(^{238}\text{Np}) t_{1/2}(^{238}\text{Np})}{\ln(2)\Phi_n R_i \varepsilon_{ij} F_{ij} N_j(^{237}\text{Np})} \tag{13}$$

The uncertainties for the weighted means were calculated using error propagation of Equation 13.

For completeness the results from all 8 γ-rays are reported here. The weighted averages of the measured ^{238}Np half-lives and the ^{237}Np$(n,\gamma)^{238}$Np integral cross sections from all 8 γ-rays were 50.27(5) hours and 339(11) mb respectively. Selecting the three γ-rays with the strongest decay branches, and therefore the highest statistics (984.6, 1026.0, and 1028.6 keV) and computing the weighted averages produced 50.31(5) hours and 342(11) mb.

This work recommends a value of 50.31(5) hours for the ^{238}Np half-life as it is the result of combining the three decay curves with the highest statistics, and due to the relatively large size of these peaks in comparison to other features in the γ-ray spectrum, any unidentified interference is likely to have had only small effect on the final result. Figure 13 shows a comparison of the measured half-life values for the Peaks 6, 7, and 8 (red circles), previous measurements of the ^{238}Np half-life (black diamonds), and the current ENSDF value (blue square). The weighted average and associated uncertainty of the Peak 6, 7, and 8 values from this work is shown as red-dotted line and corresponding shaded region. The result from this work shows excellent agreement with the ENSDF value.

The average integral cross section from all 8 γ-rays 339(11) mb, and just the three highest statistics γ-rays, 342(11) mb, agree within uncertainty. We recommend using the latter for the same reasons listed above in the half-life discussion. The results of this measurement were compared to the ENDF and JENDL evaluated ^{237}Np$(n,\gamma)^{238}$Np integral cross sections. The neutron fluence was binned into 100 neutron groups and both of the evaluated cross sections were then binned into equivalent neutron energy bins. The total ^{237}Np$(n,\gamma)^{238}$Np cross section is calculated using Equation 14, where σ_i and ϕ_i are the average cross section and neutron fluence for each neutron energy bin.

$$\sigma_{total} = \frac{\sum_k \sigma_k \phi_k}{\sum_k \phi_k} \tag{14}$$

The resulting cross sections were 354(3) mb using the ENDF evaluated cross section and 304(3) mb using the JENDL evaluated cross section. The recommended value from this measurement agrees with ENDF with overlapping 1σ error bands and is 3σ away from JENDL as shown in Figure 14. ENDF and JENDL evaluated cross sections diverge from 0.1 MeV and above such that JENDL is underestimating within this region. In order to evaluate the contribution of the dip in JENDL at around 7 MeV, we substituted JENDL's cross section above 2 MeV with ENDF. This resulted in a 4 mb increase in JENDL's cross section, which is still 3σ away from our measurement. Our measurement therefore indicates that ENDF has a better representation of the true cross section in the region of 0.1 and 2 MeV and does not rule out the structure of JENDL's cross section at around 7 MeV.

V. CONCLUSION

A measurement of the ^{237}Np$(n,\gamma)^{238}$Np integral cross section has been performed using a fast neutron

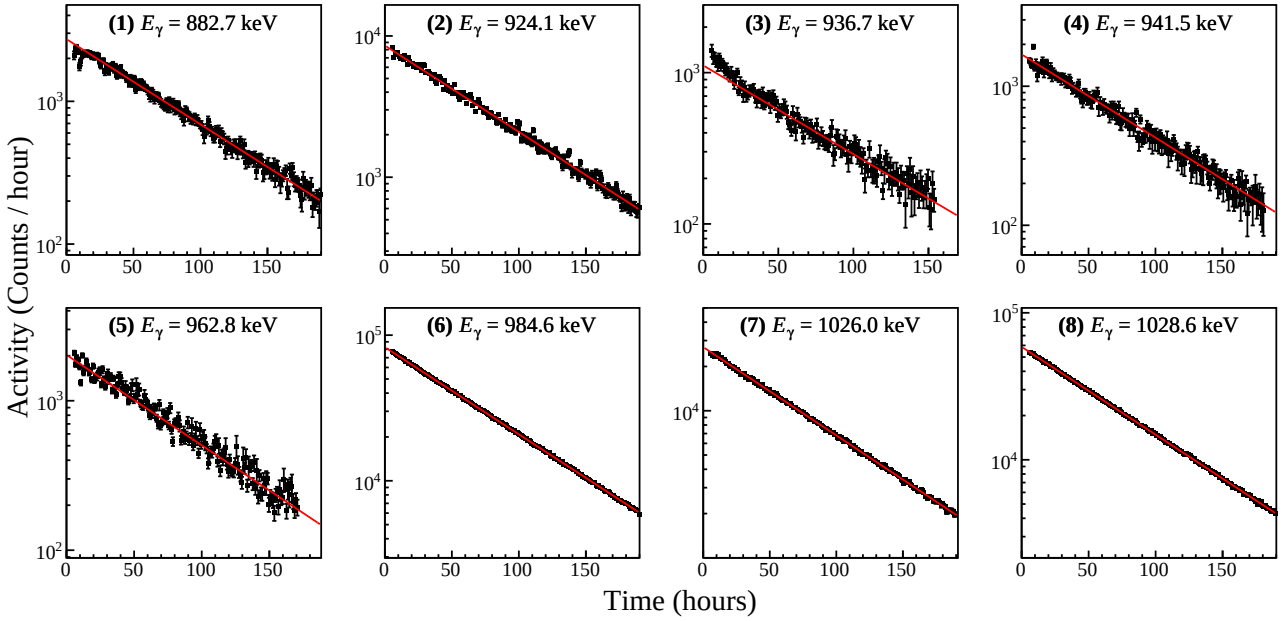

FIG. 10: The measured decay curves for the 8 γ-rays emitted in the decay of ^{238}Np that were used for this analysis. The vertical axes are counts per hour and the horizontal axes are time since irradiation in hours. The red lines are the fits to the data using Equation 9. The individual plots are numbered to match the peak labels in Figure 8 and Figure 9 and the peak number column in Table V.

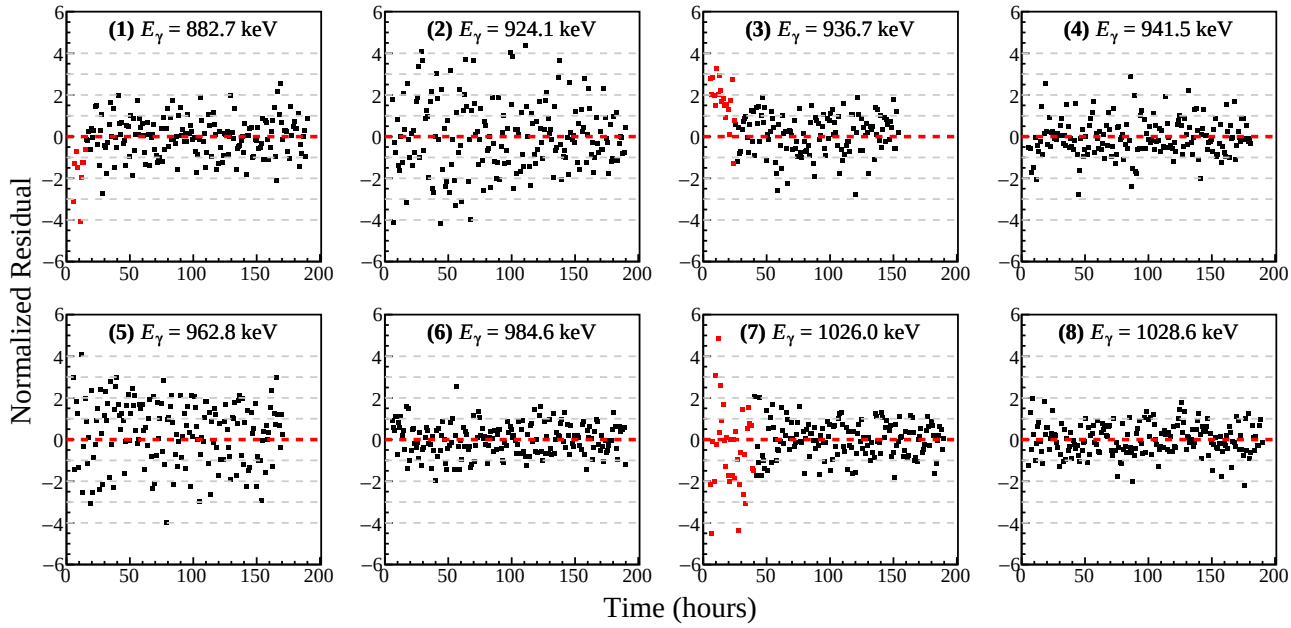

FIG. 11: The normalized residuals of the measured decay curve data and the fit using Equation 9. The red points represent regions where the data showed divergence from the expected decay curve behavior, and were therefore not included in the final fit to the data.

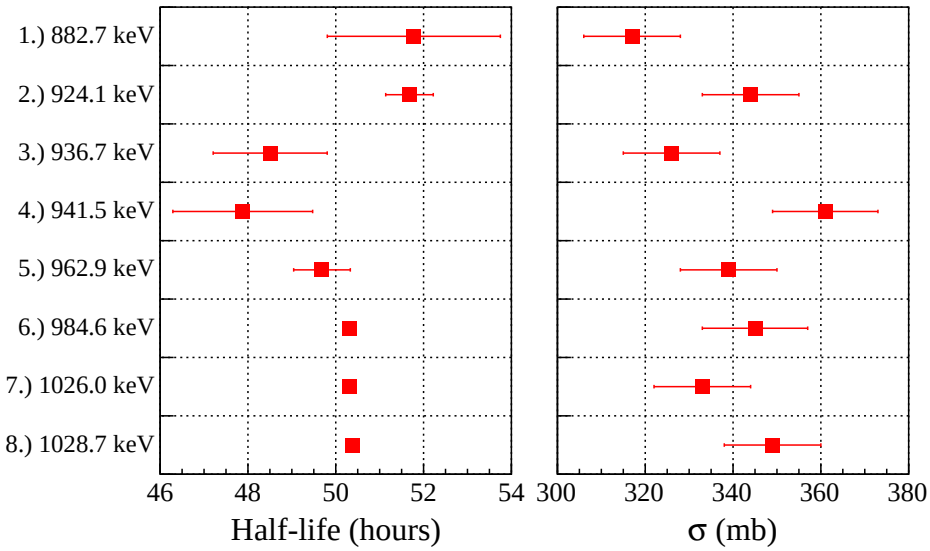

FIG. 12: The measured ^{238}Np half-life and ^{237}Np$(n,\gamma)^{238}$Np integral cross section for each of the 8 γ-rays used in this analysis.

TABLE V: The results for the half-life ($t_{1/2}$), initial activity (A_0), and integral cross section (σ) as measured with each of the 8 individual γ-rays emitted in the decay of ^{238}Np. The last row values are the uncertainty-weighted mean of the three highest energy γ-rays, resulting in a 50.31(5) h half-life and 342(11) mb integral cross section.

									$t_{1/2}$ = 50.31(5) h				
E_γ	R_γ	$t_{1/2}^{8815}$	$t_{1/2}^{8816}$	$t_{1/2}^{mean}$	ϵ_γ^{8815}	ϵ_γ^{8816}	F_{sa}^{8815}	F_{sa}^{8816}	A_0^{8815}	A_0^{8816}	σ_{8815}	σ_{8816}	σ_{mean}
(keV)	(%)	(h)	(h)	(h)	(%)	(%)	(%)	(%)	(kBq)	(kBq)	(mb)	(mb)	(mb)
882.7	0.802(7)	52(3)	52(3)	52(2)	0.3904(9)	0.3314(8)	99.4(1)	99.2(1)	23.2(5)	22.6(5)	324(14)	310(13)	317(11)
924.1	2.6634(180)[a]	50.8(7)	52.7(8)	51.7(5)	0.3783(8)	0.3213(8)	99.4(1)	99.3(1)	24.4(4)	25.3(4)	340(13)	348(14)	344(11)
936.7	0.360(3)	48(2)	49(2)	49(1)	0.3749(8)	0.3184(8)	99.4(1)	99.3(1)	23.3(4)	23.8(4)	325(13)	327(13)	326(11)
941.5	0.498(6)	48(2)	48(2)	48(2)	0.3736(8)	0.3173(7)	99.4(1)	99.3(1)	25.9(4)	26.3(5)	362(15)	361(15)	361(12)
962.9	0.644(6)	50.0(9)	49.3(9)	49.7(6)	0.3680(8)	0.3127(7)	99.5(1)	99.3(1)	24.7(3)	24.4(4)	345(13)	334(13)	339(11)
984.6	25.2(3)	50.3(1)	50.3(1)	50.32(7)	0.3626(8)	0.3081(7)	99.5(1)	99.3(1)	25.1(3)	24.8(3)	350(13)	341(13)	345(12)
1026	8.75(7)	50.1(2)	50.5(2)	50.3(1)	0.3529(8)	0.3001(7)	99.5(1)	99.4(1)	24.1(2)	24.0(2)	336(13)	329(12)	333(11)
1028.6	18.23(12)	50.4(1)	50.4(1)	50.38(8)	0.3523(8)	0.2996(7)	99.5(1)	99.4(1)	25.4(2)	25.1(2)	354(13)	345(13)	349(11)
				50.31(5)									342(11)

[a] sum of two γ-ray branching ratios of 2.598(18)% and 0.0654%.

spectrum provided by the Godiva-IV critical assembly. We measured an integral cross section of 342(11) mb for ^{237}Np$(n,\gamma)^{238}$Np. The inclusion of eight different γ-rays in the determination of the initial activity of ^{237}Np and the post-irradiation activity of ^{238}Np provides a robust measurement and benchmark for future nuclear data validation. In this work, we have also measured the ^{238}Np half-life of 50.31(5) h which is within 1σ of the current ENSDF evaluated half-life of 50.376(48) h.

Currently there is a discrepancy in the evaluations of the ^{237}Np$(n,\gamma)^{238}$Np cross section above 0.1 MeV incident neutron energy and upwards where ENDF and JENDL libraries diverge. As can be seen in Figure 14, our results support the ENDF evaluation and are more than 3σ away from the JENDL evaluation. Our result does not disprove the stucture of JENDL at around 7 MeV, but shows that JENDL underestimates the cross section between 0.1 and 2 MeV. Therefore, we recommend that users of nuclear data use the ENDF ^{237}Np$(n,\gamma)^{238}$Np cross section between 0.1 and 2 MeV and nuclear data evaluators consider this measurement during the differential cross section adjustments.

This measurement is the first measurement of integral cross sections using the Godiva-IV critical assembly and will be the first EXFOR entry for the ^{237}Np$(n,\gamma)^{238}$Np integral cross section measurement us-

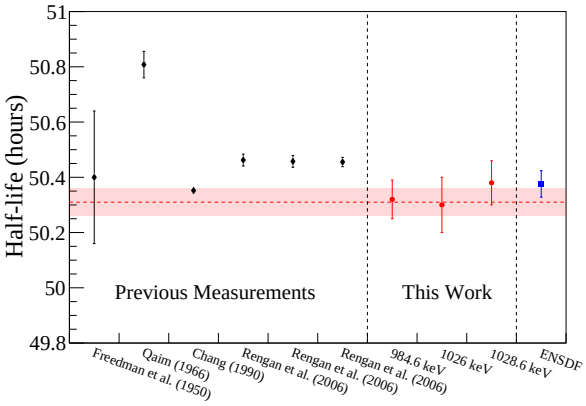

FIG. 13: Comparison of ^{238}Np half-life measurements with the three best values measured in this work. The previous measurements are shown as black diamonds, the red circles are the values measured in this work, and the blue square is the current ENSDF evaluation. The horizontal red-dotted line is the recommended value from this work and represents a weighted average of the half-life value measured with the 984.6-keV, 1026.0-keV, and 1028.6-keV γ-rays. The shaded red region around the recommended value is the corresponding uncertainty in the weight average.

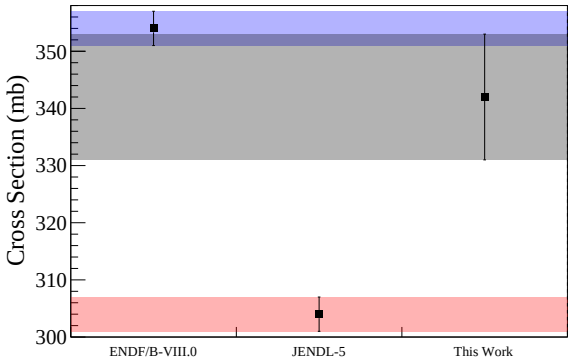

FIG. 14: Comparison of calculated integral ^{237}Np(n,γ) cross section for ENDF, JENDL, and this work. The points are accompanied with 1σ error bands.

ing a critical assembly. Godiva-IV is a high-flux neutron source with a well characterized neutron spectrum and has the ability to perform prompt irradiation, all of which make it a desirable device for conducting activation type measurements. Plans for future irradiations at LANL's Godiva-IV critical assembly are currently underway, which include a rabbit system to measure short-lived fission product yields and short-lived activation products for integral cross section measurements. A future experimental campaign using LLNL's Maui D-T generator will allow for the measurement of ^{237}Np$(n,\gamma)^{238}$Np cross section using 14 MeV neutrons.

ACKNOWLEDGMENTS

This work was funded by the Office of Defense Nuclear Nonproliferation Research and Development within the United States Department of Energy's National Nuclear Security Administration. This work was performed under the auspices of the United States Department of Energy by Lawrence Livermore National Laboratory under Contract DE-AC52-07NA27344. This work was supported by the US Department of Energy through the Los Alamos National Laboratory. Los Alamos National Laboratory is operated by Triad National Security, LLC, for the National Nuclear Security Administration of the US Department of Energy under Contract No. 89233218CNA000001. The National Criticality Experiments Research Center (NCERC), utilized in this work, is operated by Los Alamos National Laboratory and supported by the United States Department of Energy Nuclear Criticality Safety Program, funded and managed by the National Nuclear Security Administration for the Department of Energy.

[1] M. Salvatores, "Uncertainty and target accuracy assessment for innovative systems using recent covariance data evaluations," (2008).

[2] N. Otuka, E. Dupont, V. Semkova, B. Pritychenko, A. Blokhin, M. Aikawa, S. Babykina, M. Bossant, G. Chen, S. Dunaeva, R. Forrest, T. Fukahori, N. Furutachi, S. Ganesan, Z. Ge, O. Gritzay, M. Herman, S. Hlavač, K. Katō, B. Lalremruata, Y. Lee, A. Makinaga, K. Matsumoto, M. Mikhaylyukova, G. Pikulina, V. Pronyaev, A. Saxena, O. Schwerer, S. Simakov, N. Soppera, R. Suzuki, S. Takács, X. Tao, S. Taova, F. Tárkányi, V. Varlamov, J. Wang, S. Yang, V. Zerkin, and Y. Zhuang, Nuclear Data Sheets **120**, 272 (2014).

[3] É. Fomushkin, G. Novoselov, Y. I. Vinogradov, V. Vyachin, V. Gavrilov, A. Koshelev, V. Polynov, V. Surin, and A. Shvetsov, Soviet Atomic Energy **62**, 337 (1987).

[4] A. Cricchio, R. Ernstberger, L. Koch, and R. Wellum, in *Nuclear Data for Science and Technology: Proceedings of the International Conference Antwerp 6–10 September 1982* (Springer, 1983) pp. 175–177.

[5] A. Zvonarev, V. Kolyzhenkov, V. Liforov, G. Manturov, O. Matveev, I. Proshin, Y. S. Khomyakov, and A. Tsibulya, *Comparison of measured and calculated cross-sections of a large number of nuclides*, Tech. Rep. (1991).

[6] D. Heinrichs, *BR-1 Reactor Spectral Indices Benchmarks*, Tech. Rep. (Lawrence Livermore National Laboratory, Livermore CA, LLNL-TR-838379, 2022).

[7] R. Buck, E. Lent, T. Wilcox, and S. Hadjimarkos, *COG user's manual: A multiparticle Monte Carlo transport code*, Tech. Rep. (2002).

[8] D. Brown, M. Chadwick, R. Capote, A. Kahler, A. Trkov, M. Herman, A. Sonzogni, Y. Danon, A. Carlson, M. Dunn, D. Smith, G. Hale, G. Arbanas, R. Arcilla, C. Bates, B. Beck, B. Becker, F. Brown, R. Casperson, J. Conlin, D. Cullen, M.-A. Descalle, R. Firestone, T. Gaines, K. Guber, A. Hawari, J. Holmes, T. Johnson, T. Kawano, B. Kiedrowski, A. Koning, S. Kopecky, L. Leal, J. Lestone, C. Lubitz, J. Márquez Damián, C. Mattoon, E. McCutchan, S. Mughabghab, P. Navratil, D. Neudecker, G. Nobre, G. Noguere, M. Paris, M. Pigni, A. Plompen, B. Pritychenko, V. Pronyaev, D. Roubtsov, D. Rochman, P. Romano, P. Schillebeeckx, S. Simakov, M. Sin, I. Sirakov, B. Sleaford, V. Sobes, E. Soukhovitskii, I. Stetcu, P. Talou, I. Thompson, S. van der Marck, L. Welser-Sherrill, D. Wiarda, M. White, J. Wormald, R. Wright, M. Zerkle, G. Žerovnik, and Y. Zhu, Nuclear Data Sheets **148**, 1 (2018), special Issue on Nuclear Reaction Data.

[9] A. J. Plompen, O. Cabellos, C. De Saint Jean, M. Fleming, A. Algora, M. Angelone, P. Archier, E. Bauge, O. Bersillon, A. Blokhin, *et al.*, The European Physical Journal A **56**, 1 (2020).

[10] O. Iwamoto, N. Iwamoto, S. Kunieda, F. Minato, S. Nakayama, Y. Abe, K. Tsubakihara, S. Okumura, C. Ishizuka, T. Yoshida, *et al.*, journal of nuclear science and technology **60**, 1 (2023).

[11] D. C. Stupegia, M. Schmidt, and C. R. Keedy, Nuclear Science and Engineering **29**, 218 (1967).

[12] M. Lindner, R. Nagle, and J. Landrum, Nuclear Science and Engineering **59**, 381 (1976).

[13] M. Hoffman, Bull. Am. Phys. Soc. **21**, 655 (1976).

[14] L. Weston and J. Todd, Nuclear Science and Engineering **79**, 184 (1981).

[15] Y. N. Trofimov and Y. A. Nemilov, in *Proc.Conf.Neutron Physics* (1984).

[16] Y. N. Trofimov, Yadernye Konstanty (1987).

[17] N. Buleeva, A. Davletshin, A. Tipunkov, S. Tikhonov, and V. Tolstikov, Soviet Atomic Energy **65**, 920 (1988).

[18] K. Kobayashi, S. Lee, S. Yamamoto, H. J. Cho, and Y. Fujita, Journal of nuclear science and technology **39**, 111 (2002).

[19] O. Shcherbakov, K. Furutaka, S. Nakamura, H. Sakane, K. Kobayashi, S. Yamamoto, J.-I. Hori, and H. Harada, Journal of nuclear science and technology **42**, 135 (2005).

[20] E.-I. Esch, R. Reifarth, E. Bond, T. Bredeweg, A. Couture, S. Glover, U. Greife, R. Haight, A. Hatarik, R. Hatarik, *et al.*, Physical Review C **77**, 034309 (2008).

[21] K. Hirose, K. Furutaka, K. Y. Hara, H. Harada, A. Kimura, T. Kin, F. Kitatani, M. Koizumi, S. Nakamura, M. Oshima, *et al.*, journal of nuclear science and technology **50**, 188 (2013).

[22] G. Rovira, T. Katabuchi, K. Tosaka, S. Matsuura, K. Terada, O. Iwamoto, A. Kimura, S. Nakamura, N. Iwamoto, M. Segawa, *et al.*, Journal of Nuclear Science and Technology **57**, 24 (2020).

[23] G. Rovira, T. Katabuchi, K. Tosaka, S. Matsuura, Y. Kodama, H. Nakano, O. Iwamoto, A. Kimura, S. Nakamura, and N. Iwamoto, Journal of Nuclear Science and Technology **59**, 110 (2022).

[24] J. Goda, C. Bravo, T. Cutler, T. Grove, D. Hayes, J. Hutchinson, G. McKenzie, A. McSpaden, W. Myers, R. Sanchez, *et al.*, Nuclear Science and Engineering **195**, S55 (2021).

[25] K. O. Ott and R. J. Neuhold, *Introductory Nuclear Reactor Dynamics* (American Nuclear Society, 1985).

[26] T. F. Wimett, R. H. White, and R. G. Wagner, *GODIVA IV.*, Tech. Rep. LA-UR-17-29981 (Los Alamos Scientific Lab., N. Mex., 1970).

[27] R. Brun and F. Rademakers, Nuclear Instruments and Methods in Physics Research Section A: Accelerators, Spectrometers, Detectors and Associated Equipment **389**, 81 (1997).

[28] C. Werner and et al., *MCNP6.2 Release Notes*, Tech. Rep. LA-UR-18-20808 (Los Alamos National Laboratory, 2018).

[29] Greenwood, L.R. and Johnson, C.D., EPJ Web of Conferences **106**, 07001 (2016).

[30] A. Nouri, P. Nagel, J. B. Briggs, and T. Ivanova, Nuclear Science and Engineering **145**, 11 (2003).

[31] E. M. Zsolnay, R. Capote Noy, H. J. Nolthenius, and A. Trkov, *Summary description of the new international reactor dosimetry and fusion file (IRDFF release 1.0)*, Tech. Rep. INDC(NDS)-0616 (International Atomic Energy Agency, 2012).

[32] A. Trkov, P. Griffin, S. Simakov, L. Greenwood, K. Zolotarev, R. Capote, D. Aldama, V. Chechev, C. Destouches, A. Kahler, C. Konno, M. Koštál, M. Majerle, E. Malambu, M. Ohta, V. Pronyaev, V. Radulović, S. Sato, M. Schulc, E. Šimečková, I. Vavtar, J. Wagemans, M. White, and H. Yashima, Nuclear Data Sheets **163**, 1 (2020).

[33] M. Berger, J. Hubbell, S. Seltzer, J. Chang, J. Coursey, R. Sukumar, D. Zucker, and K. Olsen, *XCOM: Photon Cross Section Database* (version 1.5) [Online] Available: http://physics.nist.gov/xcom [Accessed : February 27, 2020]. National Institute of Standards and Technology, Gaithersburg, MD.

Appendix A: Detector Efficiency Error Analysis

The error band of the detector efficiency was calculated using error propagation. A covariance matrix was calculated in the form:

$$\begin{bmatrix} \Delta P_0^2 & \Delta P_{01} & \Delta P_{02} & \Delta P_{03} & \Delta P_{04} \\ \Delta P_{10} & \Delta P_1^2 & \Delta P_{12} & \Delta P_{13} & \Delta P_{14} \\ \Delta P_{20} & \Delta P_{21} & \Delta P_2^2 & \Delta P_{23} & \Delta P_{24} \\ \Delta P_{30} & \Delta P_{31} & \Delta P_{32} & \Delta P_3^2 & \Delta P_{34} \\ \Delta P_{40} & \Delta P_{41} & \Delta P_{42} & \Delta P_{43} & \Delta P_4^2 \end{bmatrix},$$

where $\Delta P_k^2 = \Delta P_{kk}$. The error propagation for Equation 2 is then:

$$\Delta\varepsilon(E_\gamma) = \sqrt{\sum_i \sum_j \frac{\delta\varepsilon(E_\gamma)}{\delta P_i}\frac{\delta\varepsilon(E_\gamma)}{\delta P_j}\Delta P_{ij}} \tag{A1}$$

where $\delta\varepsilon(E_\gamma)/\delta P_k$ are partial derivatives of $\varepsilon(E_\gamma)$ with respect to P_k. The partial derivatives of $\varepsilon(E_\gamma)$ are the following equations:

$$\frac{\delta\varepsilon(E_\gamma)}{\delta P_0} = E_\gamma^{-P_1} \tag{A2}$$

$$\frac{\delta\varepsilon(E_\gamma)}{\delta P_1} = -\ln(E_\gamma) P_0 E_\gamma^{-P_1} \tag{A3}$$

$$\frac{\delta\varepsilon(E_\gamma)}{\delta P_2} = 1 \tag{A4}$$

$$\frac{\delta\varepsilon(E_\gamma)}{\delta P_3} = -e^{-P_4 E_\gamma} \tag{A5}$$

$$\frac{\delta\varepsilon(E_\gamma)}{\delta P_4} = E_\gamma P_3 e^{-P_4 E_\gamma} \tag{A6}$$

Equation A1 is expanded to the following:

$$\begin{aligned}
\Delta\varepsilon(E_\gamma)^2 = {} & \left(\frac{\delta\varepsilon(E_\gamma)}{\delta P_0}\right)^2 \Delta P_0^2 + \left(\frac{\delta\varepsilon(E_\gamma)}{\delta P_1}\right)^2 \Delta P_1^2 \\
& + \left(\frac{\delta\varepsilon(E_\gamma)}{\delta P_2}\right)^2 \Delta P_2^2 + \left(\frac{\delta\varepsilon(E_\gamma)}{\delta P_3}\right)^2 \Delta P_3^2 \\
& + \left(\frac{\delta\varepsilon(E_\gamma)}{\delta P_4}\right)^2 \Delta P_4^2 \\
& + 2\frac{\delta\varepsilon(E_\gamma)}{\delta P_0}\frac{\delta\varepsilon(E_\gamma)}{\delta P_1}\Delta P_{01} + 2\frac{\delta\varepsilon(E_\gamma)}{\delta P_0}\frac{\delta\varepsilon(E_\gamma)}{\delta P_2}\Delta P_{02} \\
& + 2\frac{\delta\varepsilon(E_\gamma)}{\delta P_0}\frac{\delta\varepsilon(E_\gamma)}{\delta P_3}\Delta P_{03} + 2\frac{\delta\varepsilon(E_\gamma)}{\delta P_0}\frac{\delta\varepsilon(E_\gamma)}{\delta P_4}\Delta P_{04} \\
& + 2\frac{\delta\varepsilon(E_\gamma)}{\delta P_1}\frac{\delta\varepsilon(E_\gamma)}{\delta P_2}\Delta P_{12} + 2\frac{\delta\varepsilon(E_\gamma)}{\delta P_1}\frac{\delta\varepsilon(E_\gamma)}{\delta P_3}\Delta P_{13} \\
& + 2\frac{\delta\varepsilon(E_\gamma)}{\delta P_1}\frac{\delta\varepsilon(E_\gamma)}{\delta P_4}\Delta P_{14} \\
& + 2\frac{\delta\varepsilon(E_\gamma)}{\delta P_2}\frac{\delta\varepsilon(E_\gamma)}{\delta P_3}\Delta P_{23} + 2\frac{\delta\varepsilon(E_\gamma)}{\delta P_2}\frac{\delta\varepsilon(E_\gamma)}{\delta P_4}\Delta P_{24} \\
& + 2\frac{\delta\varepsilon(E_\gamma)}{\delta P_3}\frac{\delta\varepsilon(E_\gamma)}{\delta P_4}\Delta P_{34}
\end{aligned}$$

where $\Delta\varepsilon(E_\gamma)$ is used to calculate the uncertainty of the detector efficiency function.

Appendix B: Neutron Group Values

Tables VI and VII contain the information about the group-wise neutron fluence and cross sections used in the calculations presented in Section IV of this article.

Group Number	E_n Low (MeV)	E_n High (MeV)	Group Flux (n/cm^2)	ENDF (b)	JENDL (b)
1	1.00×10^{-10}	1.00×10^{-9}	1.941×10^{-7}	1.419×10^{3}	9.688×10^{3}
2	1.00×10^{-9}	1.00×10^{-8}	1.941×10^{-7}	4.446×10^{2}	4.391×10^{2}
3	1.00×10^{-8}	2.30×10^{-8}	1.942×10^{-7}	2.272×10^{2}	2.238×10^{2}
4	2.30×10^{-8}	5.00×10^{-8}	1.943×10^{-7}	1.472×10^{2}	1.441×10^{2}
5	5.00×10^{-8}	7.60×10^{-8}	1.945×10^{-7}	1.066×10^{2}	1.033×10^{2}
6	7.60×10^{-8}	1.15×10^{-7}	1.947×10^{-7}	8.303×10^{1}	8.038×10^{1}
7	1.15×10^{-7}	1.70×10^{-7}	1.950×10^{-7}	6.635×10^{1}	6.414×10^{1}
8	1.70×10^{-7}	2.55×10^{-7}	1.954×10^{-7}	5.742×10^{1}	5.581×10^{1}
9	2.55×10^{-7}	3.80×10^{-7}	1.958×10^{-7}	7.537×10^{1}	7.508×10^{1}
10	3.80×10^{-7}	5.50×10^{-7}	1.963×10^{-7}	8.353×10^{2}	8.285×10^{2}
11	5.50×10^{-7}	8.40×10^{-7}	1.969×10^{-7}	6.073×10^{1}	5.600×10^{1}
12	8.40×10^{-7}	1.28×10^{-6}	1.975×10^{-7}	4.094×10^{1}	3.988×10^{1}
13	1.28×10^{-6}	1.90×10^{-6}	1.981×10^{-7}	4.109×10^{2}	4.058×10^{2}
14	1.90×10^{-6}	2.80×10^{-6}	1.988×10^{-7}	2.218×10^{1}	2.154×10^{1}
15	2.80×10^{-6}	4.25×10^{-6}	2.790×10^{7}	9.501×10^{1}	9.433×10^{1}
16	4.25×10^{-6}	6.30×10^{-6}	2.002×10^{-7}	1.197×10^{2}	1.180×10^{2}
17	6.30×10^{-6}	9.20×10^{-6}	2.009×10^{-7}	4.777×10^{1}	4.783×10^{1}
18	9.20×10^{-6}	1.35×10^{-5}	1.081×10^{8}	1.484×10^{2}	1.502×10^{2}
19	1.35×10^{-5}	2.10×10^{-5}	2.021×10^{-7}	4.326×10^{1}	5.599×10^{1}
20	2.10×10^{-5}	3.00×10^{-5}	9.383×10^{6}	1.022×10^{2}	1.199×10^{2}
21	3.00×10^{-5}	4.50×10^{-5}	2.029×10^{-7}	5.193×10^{1}	6.481×10^{1}
22	4.50×10^{-5}	6.90×10^{-5}	2.031×10^{-7}	7.405×10^{1}	8.717×10^{1}
23	6.90×10^{-5}	1.00×10^{-4}	2.031×10^{-7}	4.511×10^{1}	5.788×10^{1}
24	1.00×10^{-4}	1.35×10^{-4}	2.232×10^{7}	3.136×10^{1}	4.056×10^{1}
25	1.35×10^{-4}	1.70×10^{-4}	6.674×10^{7}	2.669×10^{1}	3.584×10^{1}
26	1.70×10^{-4}	2.20×10^{-4}	3.533×10^{7}	2.860×10^{1}	3.702×10^{1}
27	2.20×10^{-4}	2.80×10^{-4}	3.059×10^{8}	2.498×10^{1}	3.176×10^{1}
28	2.80×10^{-4}	3.60×10^{-4}	2.693×10^{8}	1.939×10^{1}	2.503×10^{1}
29	3.60×10^{-4}	4.50×10^{-4}	1.565×10^{8}	1.582×10^{1}	2.074×10^{1}
30	4.50×10^{-4}	5.75×10^{-4}	5.612×10^{8}	1.561×10^{1}	1.664×10^{1}
31	5.75×10^{-4}	7.60×10^{-4}	8.967×10^{8}	1.427×10^{1}	1.322×10^{1}
32	7.60×10^{-4}	9.60×10^{-4}	1.786×10^{9}	1.242×10^{1}	1.140×10^{1}
33	9.60×10^{-4}	1.28×10^{-3}	3.035×10^{9}	1.076×10^{1}	9.812×10^{0}
34	1.28×10^{-3}	1.60×10^{-3}	2.890×10^{9}	9.346×10^{0}	8.518×10^{0}
35	1.60×10^{-3}	2.00×10^{-3}	2.882×10^{9}	8.255×10^{0}	7.513×10^{0}
36	2.00×10^{-3}	2.70×10^{-3}	7.211×10^{9}	7.159×10^{0}	6.500×10^{0}
37	2.70×10^{-3}	3.40×10^{-3}	9.592×10^{9}	6.206×10^{0}	5.641×10^{0}
38	3.40×10^{-3}	4.50×10^{-3}	1.875×10^{10}	5.421×10^{0}	4.939×10^{0}
39	4.50×10^{-3}	5.50×10^{-3}	2.172×10^{10}	4.802×10^{0}	4.373×10^{0}
40	5.50×10^{-3}	7.20×10^{-3}	4.831×10^{10}	4.258×10^{0}	3.906×10^{0}
41	7.20×10^{-3}	9.20×10^{-3}	6.604×10^{10}	3.726×10^{0}	3.484×10^{0}
42	9.20×10^{-3}	1.20×10^{-2}	1.259×10^{11}	3.296×10^{0}	3.138×10^{0}
43	1.20×10^{-2}	1.50×10^{-2}	1.534×10^{11}	2.983×10^{0}	2.877×10^{0}
44	1.50×10^{-2}	1.90×10^{-2}	2.315×10^{11}	2.696×10^{0}	2.652×10^{0}
45	1.90×10^{-2}	2.55×10^{-2}	5.254×10^{11}	2.390×10^{0}	2.429×10^{0}
46	2.55×10^{-2}	3.20×10^{-2}	5.789×10^{11}	2.146×10^{0}	2.226×10^{0}
47	3.20×10^{-2}	4.00×10^{-2}	8.561×10^{11}	1.964×10^{0}	2.055×10^{0}
48	4.00×10^{-2}	5.25×10^{-2}	1.606×10^{12}	1.782×10^{0}	1.851×10^{0}
49	5.25×10^{-2}	6.60×10^{-2}	1.962×10^{12}	1.600×10^{0}	1.662×10^{0}
50	6.60×10^{-2}	8.80×10^{-2}	3.810×10^{12}	1.393×10^{0}	1.411×10^{0}

TABLE VI: Neutron table part 1.

Group Number	E_n Low (MeV)	E_n High (MeV)	Group Flux (n/cm^2)	ENDF (b)	JENDL (b)
51	8.80×10^{-2}	1.10×10^{-1}	4.143×10^{12}	1.219×10^{0}	1.215×10^{0}
52	1.10×10^{-1}	1.35×10^{-1}	5.281×10^{12}	1.076×10^{0}	9.947×10^{-1}
53	1.35×10^{-1}	1.60×10^{-1}	5.317×10^{12}	9.591×10^{-1}	8.636×10^{-1}
54	1.60×10^{-1}	1.90×10^{-1}	6.787×10^{12}	8.736×10^{-1}	7.833×10^{-1}
55	1.90×10^{-1}	2.20×10^{-1}	6.594×10^{12}	8.081×10^{-1}	7.262×10^{-1}
56	2.20×10^{-1}	2.55×10^{-1}	7.589×10^{12}	7.560×10^{-1}	6.559×10^{-1}
57	2.55×10^{-1}	2.90×10^{-1}	7.480×10^{12}	7.113×10^{-1}	6.126×10^{-1}
58	2.90×10^{-1}	3.20×10^{-1}	6.411×10^{12}	6.760×10^{-1}	5.555×10^{-1}
59	3.20×10^{-1}	3.60×10^{-1}	8.249×10^{12}	6.371×10^{-1}	5.036×10^{-1}
60	3.60×10^{-1}	4.00×10^{-1}	8.008×10^{12}	5.794×10^{-1}	4.360×10^{-1}
61	4.00×10^{-1}	4.50×10^{-1}	9.315×10^{12}	5.123×10^{-1}	3.767×10^{-1}
62	4.50×10^{-1}	5.00×10^{-1}	8.973×10^{12}	4.453×10^{-1}	3.347×10^{-1}
63	5.00×10^{-1}	5.50×10^{-1}	8.472×10^{12}	3.860×10^{-1}	2.874×10^{-1}
64	5.50×10^{-1}	6.00×10^{-1}	8.071×10^{12}	3.363×10^{-1}	2.494×10^{-1}
65	6.00×10^{-1}	6.60×10^{-1}	9.046×10^{12}	2.952×10^{-1}	2.136×10^{-1}
66	6.60×10^{-1}	7.20×10^{-1}	8.386×10^{12}	2.607×10^{-1}	1.831×10^{-1}
67	7.20×10^{-1}	7.80×10^{-1}	7.657×10^{12}	2.335×10^{-1}	1.628×10^{-1}
68	7.80×10^{-1}	8.40×10^{-1}	7.082×10^{12}	2.130×10^{-1}	1.448×10^{-1}
69	8.40×10^{-1}	9.20×10^{-1}	8.583×10^{12}	1.966×10^{-1}	1.309×10^{-1}
70	9.20×10^{-1}	1.00×10^{0}	7.907×10^{12}	1.807×10^{-1}	1.204×10^{-1}
71	1.00×10^{0}	1.20×10^{0}	1.718×10^{13}	1.483×10^{-1}	1.069×10^{-1}
72	1.20×10^{0}	1.40×10^{0}	1.431×10^{13}	1.141×10^{-1}	8.950×10^{-2}
73	1.40×10^{0}	1.60×10^{0}	1.218×10^{13}	9.193×10^{-2}	7.562×10^{-2}
74	1.60×10^{0}	1.80×10^{0}	1.055×10^{13}	7.629×10^{-2}	6.396×10^{-2}
75	1.80×10^{0}	2.00×10^{0}	9.087×10^{12}	6.575×10^{-2}	5.422×10^{-2}
76	2.00×10^{0}	2.30×10^{0}	1.157×10^{13}	5.419×10^{-2}	4.298×10^{-2}
77	2.30×10^{0}	2.60×10^{0}	9.531×10^{12}	4.400×10^{-2}	3.176×10^{-2}
78	2.60×10^{0}	2.90×10^{0}	7.845×10^{12}	3.659×10^{-2}	2.277×10^{-2}
79	2.90×10^{0}	3.30×10^{0}	8.302×10^{12}	3.131×10^{-2}	1.559×10^{-2}
80	3.30×10^{0}	3.70×10^{0}	6.357×10^{12}	2.656×10^{-2}	9.861×10^{-3}
81	3.70×10^{0}	4.10×10^{0}	4.857×10^{12}	2.266×10^{-2}	6.415×10^{-3}
82	4.10×10^{0}	4.50×10^{0}	3.698×10^{12}	1.927×10^{-2}	4.288×10^{-3}
83	4.50×10^{0}	5.00×10^{0}	3.409×10^{12}	1.649×10^{-2}	2.807×10^{-3}
84	5.00×10^{0}	5.50×10^{0}	2.429×10^{12}	1.385×10^{-2}	1.885×10^{-3}
85	5.50×10^{0}	6.00×10^{0}	1.712×10^{12}	1.206×10^{-2}	1.396×10^{-3}
86	6.00×10^{0}	6.70×10^{0}	1.579×10^{12}	1.049×10^{-2}	1.113×10^{-3}
87	6.70×10^{0}	7.40×10^{0}	9.449×10^{11}	9.083×10^{-3}	1.054×10^{-3}
88	7.40×10^{0}	8.20×10^{0}	6.337×10^{11}	7.900×10^{-3}	1.177×10^{-3}
89	8.20×10^{0}	9.00×10^{0}	3.559×10^{11}	6.838×10^{-3}	1.340×10^{-3}
90	9.00×10^{0}	1.00×10^{1}	2.383×10^{11}	6.000×10^{-3}	1.537×10^{-3}
91	1.00×10^{1}	1.10×10^{1}	1.178×10^{11}	5.190×10^{-3}	1.634×10^{-3}
92	1.10×10^{1}	1.20×10^{1}	5.730×10^{10}	4.580×10^{-3}	1.610×10^{-3}
93	1.20×10^{1}	1.30×10^{1}	2.767×10^{10}	4.060×10^{-3}	1.528×10^{-3}
94	1.30×10^{1}	1.40×10^{1}	1.300×10^{10}	3.660×10^{-3}	1.357×10^{-3}
95	1.40×10^{1}	1.50×10^{1}	5.626×10^{9}	3.310×10^{-3}	1.133×10^{-3}
96	1.50×10^{1}	1.60×10^{1}	3.139×10^{9}	3.020×10^{-3}	9.112×10^{-4}
97	1.60×10^{1}	1.70×10^{1}	1.336×10^{9}	2.775×10^{-3}	7.554×10^{-4}
98	1.70×10^{1}	1.80×10^{1}	4.843×10^{8}	2.570×10^{-3}	6.424×10^{-4}
99	1.80×10^{1}	1.90×10^{1}	4.707×10^{8}	2.375×10^{-3}	5.627×10^{-4}
100	1.90×10^{1}	2.00×10^{1}	1.094×10^{8}	2.200×10^{-3}	5.060×10^{-4}

TABLE VII: Neutron table part 2.